Structure and Piezoelectricity Due to B Site Cation Variation in $AB^{n+}Cl_{n+2}$ Hybrid Histammonium Chlorometallate Materials

Michael Wells,[a] Jacob Hempel,[b] Santosh Adhikari,[c] Qingping Wang,[d] Daniel Allen,[a] Alison Costello,[a] Chris Bowen,[d] Sean Parkin,[a] Christopher Sutton,[c] Aron J. Huckaba[a*]

a: Department of Chemistry, University of Kentucky, Lexington, KY 40506, United States.

b: Department of Physics and Astronomy, University of Kentucky, Lexington, KY 40506, United States.

c: Department of Chemistry and Biochemistry, University of South Carolina, Columbia, SC, 29208, United States.

d: Department of Mechanical Engineering, University of Bath, Bath, BA2 7AY, United Kingdom.

*Corresponding author. Email: aron.huckaba@uky.edu

Abstract

To provide new insights in understanding the influence of B site cation on structure in chlorometallate materials of the form $AB^{n+}Cl_{n+2}$, we report novel organic-inorganic hybrid

metallates (OIHM) incorporating histammonium ($HistNH_3$) dications and various transition metal and main group B site cations. Single crystals of OIHMs with the basic formula ($HistNH_3M^{n+}Cl_{n+2}$, M = Fe, Co, Ni, Cu, Zn, Cd, Hg, Sb, Sn, Pb, Bi) were grown and their structures characterized by single crystal X-ray crystallography. $HistNH_3CoCl_4$, $HistNH_3ZnCl_4$, and $HistNH_3SbCl_5$ crystallized in a non-centrosymmetric space group and were subsequently studied with piezoresponse force microscopy (PFM). While bulk measurements of crystals and poly(vinylidene difluoride) (PVDF)/metallate composite films exhibited low bulk response values, surface measured local response values from PFM of 5.17 pm/V for $HistNH_3CoCl_4$, 22.6 pm/V for $HistNH_3ZnCl_4$, and 2.9 pm/V for $HistNH_3SbCl_5$, compared with 2.50 pm/V for PVDF reference samples. The magnitude of d33 coefficient, net dipole, and cation-Cl bond dipole obtained from the density functional theory calculations confirm the higher response in $HistNH_3ZnCl_4$ compared to $HistNH_3CoCl_4$. Density of states and crystal orbital Hamilton population analysis indicate that the higher net dipole in $HistNH_3ZnCl_4$ compared to $HistNH_3CoCl_4$ is due to the lower hybridization of the M-Cl bond.

Introduction

Hybrid Organic Inorganic Metallates (OIHMs) are an important class of crystalline materials that are low temperature and solution processable, and are increasingly being studied in photovoltaics,[1] light emitting diodes,[2] lasers,[3] and photodetectors.[4] Thin film and single crystal OIHMs are relatively easy to synthesize,[5, 6] and a wide variety of A site cations have been utilized in 3-D lead halide halometallates (also termed perovskites in their 3-D and quasi-2-D forms) of the form ABX_3, where A is an organic cation, B is a divalent lead cation, and X is a halide anion like I^- ,

Br^-, or Cl^-.[7] If the cation is too large to fit within the interstitial spaces between BX_6 octahedra, halide sharing between octahedra will decrease to allow for effective charge compensation between A and B site cations and the structure then turns into a 2-D structure.[8] A further decrease in halide sharing to just one corner, edge, or facial halide sharing interaction between metal centers can lead to a 1-D structure, while the absence of any halide sharing leads to a 0-D structure.[9-11]

While there have been many studies on 3-D, quasi 2-D, and 2-D perovskite systems, less work has been undertaken on the "molecular" 1-D or 0-D systems, that is, those materials with intrinsically separated metal halide anions. It can certainly be argued in these materials that they could be more accurately called by the more general name halometallate, instead of perovskite, which others have also suggested.[12] Therefore, for the rest of this work we will refer to materials of the formula $AB^{n+}X_{n+2}$ as hybrid organic inorganic halometallates.

The approach here was to utilize hybrid organic-inorganic halometallates with a dication, histammonium dichloride ($HistNH_3$), which has two different cation moieties, one primary ammonium cation and one imidazolium cation. Since the two cations have different steric profiles and vastly different hydrogen-bonding patterns, major differences in cation placement within the crystalline framework was expected, and we hypothesized that upon changing the B-site cation identity it would be possible to synthesize metallate materials that crystallize in lower symmetry space groups.

In this work, we report the single-crystal X-ray structures of many novel organic-inorganic hybrid metalate (OIHM) materials and the piezoelectric characteristics of a few, namely materials based on Zn, Co, and Sb. Single crystalline samples of these three materials exhibited piezoelectric properties, however, $HistNH_3ZnCl_4$ displayed the highest overall piezoelectric response even

though it is isostructural with $HistNH_3CoCl_4$. Theoretical studies and literature data of the two materials indicated that the difference in response was found to be due to the difference in magnitude of the material dipole and M-Cl dipole.

Results & Discussion

Material Synthesis and Crystallographic Analysis

Organic Inorganic Hybrid Materials (OIHMs) were synthesized here, $HistNH_3M^{n+}Cl_{n+2}$, where $HistNH_3$ = histammonium and M = Fe^{2+}, Fe^{3+}, Co, Ni, Cu, Zn, Cd, Hg, Sn, Pb, Sb, and Bi by mixing equimolar quantities of histammonium dichloride and metal chloride in either concentrated HCl, water acidified with HCl, water/methanol mixtures acidified with HCl, or DMSO. Either slow evaporation of the solution or slow cooling of a concentrated solution led to the growth of X-ray quality single crystals. We started by screening the first row of the transition metals and found much variability in material crystalline structure.

A pale orange $HistNH_3FeCl_4$ material crystallized from an equimolar mixture of $FeCl_2$ and histammonium dihydrochloride (**Figure 1a**) in a centrosymmetric space group ($P2_1/c$) and in stacked networks of a typical 0-D structure, with distorted metal-trigonal pyramidal dianions separated by histamine dications.

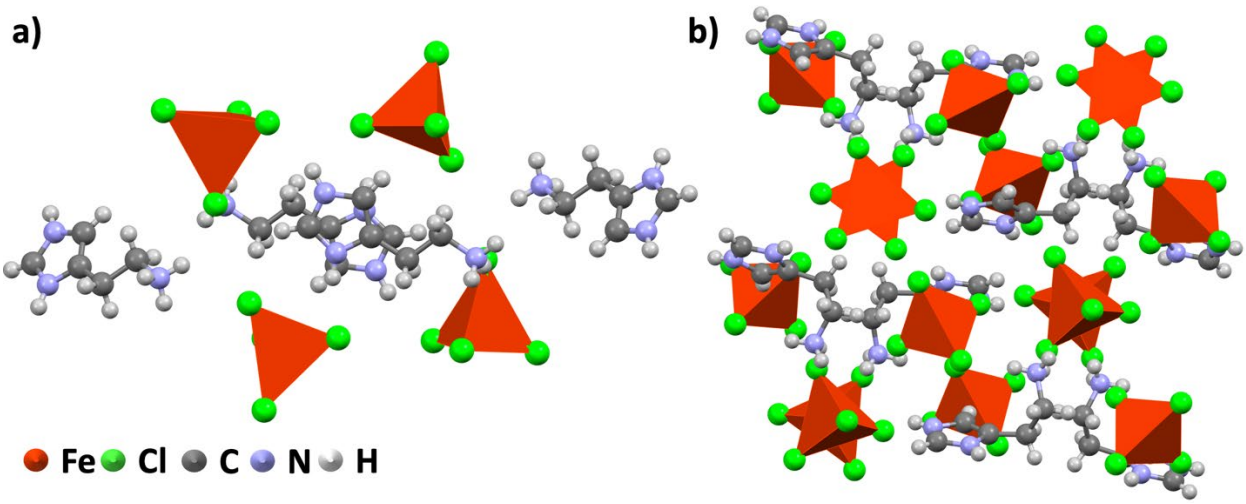

Figure 1. Crystallographically determined X-ray structures of (a) $HistNH_3FeCl_4$ and (b) $HistNH_3(FeCl_4)_2$.

Each Fe center is bonded to four Cl ligands, with three shorter Fe-Cl bonds (between 2.2826 and 2.3480 Å), and one longer Fe-Cl bond (2.4091 Å). There were three smaller Cl…Fe…Cl bond angles (98.44, 99.32, and 101.73º), two angles at 112.73º and 113.35º, and one larger angle of 125.23º. In each unit cell, there are four MCl_4 and four histammonium molecules, a total of 5 hydrogen bonding interactions per histammonium, to yield 20 hydrogen-bonding interactions within and between each unit cell. The bond angles observed here for $[FeCl_4]^{2-}$ are substantially different than those observed in past studies on $FeCl_4$ OIHM materials, in which each exhibited a tetrahedral geometry.[13-16]

When $FeCl_3$ was combined with histamine in an equimolar ratio, we aimed to form $FeCl_5$ dianions, however, a yellow $HistNH_3(FeCl_4)_2$ material crystallized (**Figure 1b**) in a centrosymmetric space group (*Pbca*). The $HistNH_3(FeCl_4)_2$ was comprised of two distorted $[FeCl_4]^-$ anion tetrahedra that are charge balanced by the histammonium dication. All eight Fe-Cl bond lengths are similar, and range between 2.1833 Å and 2.2119 Å. The Cl…Fe…Cl bond angles range from 105.74º at the smallest to 112.67º. Only one hydrogen-bonding interaction is present

in each charge balanced structure, between the NH_3 cation and one of the Cl ligands. The $FeCl_4$ dianions in this structure were typical distorted tetrahedra, in comparison to other $Fe^{III}Cl_4$ tetrahedra.[13]

Both colorless $HistNH_3ZnCl_4$ and deep blue $HistNH_3CoCl_4$ materials are isostructural (**Figure 2a, 2b**) and were both found to crystallize from an equimolar mixture of MCl_2 (M=Co, Zn) and histammonium dihydrochloride in a non-centrosymmetric space group (*Pna2₁*), in a stacked network of a 0-D structure. We had previously grown crystals of $HistNH_3ZnCl_4$ studied its mechanochemical properties by nanoindentation measurements,[17] and during the course of the current work discovered that others had reported the crystal structures of $HistNH_3ZnCl_4$ and $HistNH_3CoCl_4$ before.[18, 19]

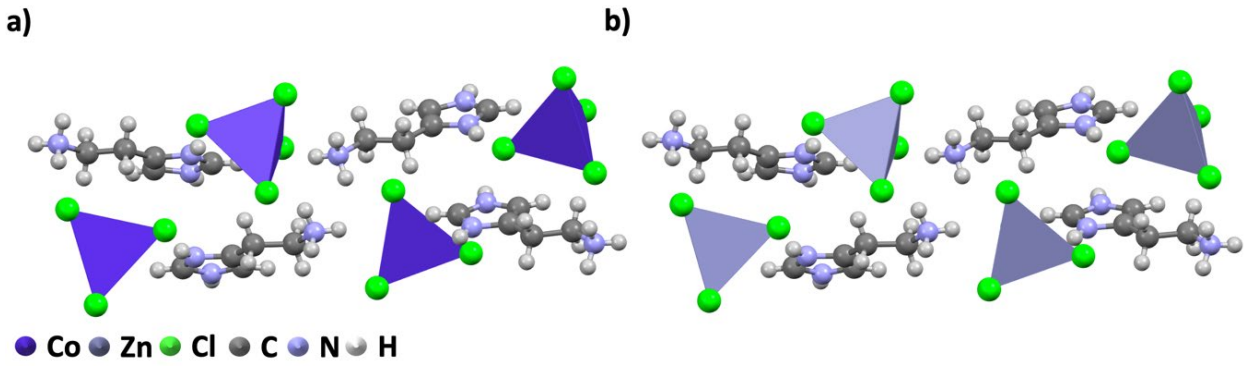

Figure 2. Crystallographically determined X-ray structures of (a) $HistNH_3CoCl_4$ and (b) $HistNH_3ZnCl_4$.

They are comprised of individual metal atoms bonded to four (4) chloride ions that yield a tetrahedral dianionic chlorometallate that is charge-balanced by the dicationic histammonium.[19] The M-Cl bond distances range from 2.2540 Å to 2.2891 Å when M = Zn and from 2.2589 Å to 2.2883 Å when M = Co. There are two Cl-M-Cl bond angles that are below the ideal tetrahedron angles (106.64º and 107.24º when M = Zn and 106.20º and 107.94º when M = Co) and two that are above (111.15º and 114.16º when M = Zn and 111.95º and 114.67º when M = Co). The

imidazolium cations pack to maximize π-π interactions and are spaced ~3.57 Å, with the ammonium cations packing as far as possible from the other cations. Each MCl_4 (M=Zn, Co) anionic tetrahedron participates in three hydrogen bonds: one of the Cl ligands participates in two hydrogen bonding interactions with two separate histammonium imidazole N-H groups, with an N…Cl…N H-bond angle of ~156º and a hydrogen bond distance of ~3.13 Å, while the Cl ligand nearest the first one participates in a hydrogen bond interaction with a nearby histammonium amine N-H group with a hydrogen bond distance of ~3.21 Å. In each unit cell, there are four MCl_4 tetrahedra, four histammonium molecules, and in $HistNH_3ZnCl_4$ and $HistNH_3CoCl_4$ a total of 3 hydrogen bonding interactions per histammonium, for a total of 12 hydrogen-bonding interactions within and between each unit cell. The structural parameters of both materials were similar to other $Zn^{II}Cl_4$ and $Co^{II}Cl_4$ tetrahedra reported in the literature.[20-24]

The yellow $HistNH_3Ni(H_2O)Cl_4$ material crystallized from an equimolar mixture of $NiCl_2$ and histammonium dihydrochloride (**Figure 3a**) in a centrosymmetric space group ($P2_1/c$), however the crystals were 4-fold twinned by pseudo-merohedry.[25]

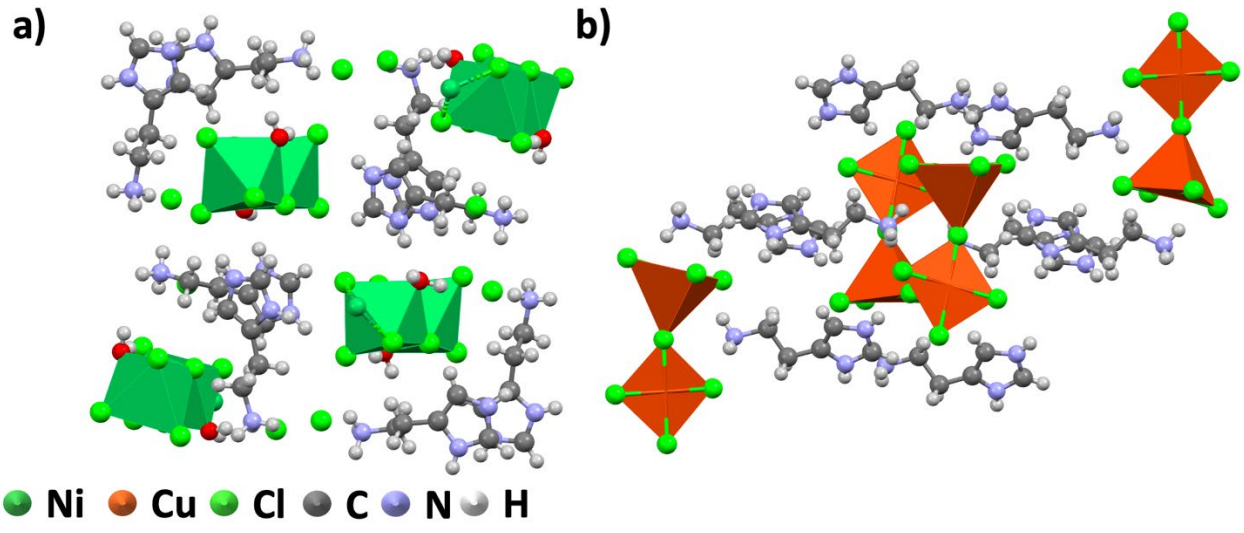

Figure 3. Crystallographically determined X-ray structures of (a) $[HistNH_3Ni(H_2O)Cl_3]Cl$ and (b) $HistNH_3CuCl_4$.

They exhibited stacked networks of a typical 1-D structure, with metal octahedra extending in long charge-compensated wires. Atypical in this structure, however, is the inclusion of a water molecule coordinated to each Ni center, as is the presence of an uncoordinated Cl ion. The Cl ion is situated near to the coordinated water. In the wires, the Ni…Ni bond distances alternate between 3.446 Å and 3.456 Å, the Ni-Cl bond distances for the shared Cl ligands are 2.394 Å on average, while the unshared Ni-Cl bond has a length of 2.412 Å. The Ni-O bond distance in the wires is 2.132 Å, and the N-Cl distance between the ammonium cation and the Cl ion is 3.681 Å. The ammonium cations are situated towards other ammonium cations and Cl ions and the imidazolium cation is oriented between the $NiCl_5(H_2O)$ wires with π-π stacking between imidazolium subunits, with a total of 27 hydrogen-bonding interactions within and between each unit cell. Others have observed other types of linear 1-D chloronickelates,[26] chloronickelates with Cl and OH_2 ligands,[27] but the most commonly observed chloronickelate geometry is tetrahedral.[28-30]

The green $HistNH_3CuCl_4$ material crystallized from an equimolar mixture of $CuCl_2$ and histammonium dihydrochloride (**Figure 3b**) in a centrosymmetric space group ($P2_1/c$), but were non-merohedric twins.[25] They exhibited a unique structure, incorporating one square-planar and one square-pyramidal metal center linked through a bridging chloride ligand with a Cu…Cl…Cu bond angle of 163.16º. In the square pyramidal Cu center one longer Cu-Cl bond (2.3093 Å), two medium Cu-Cl bonds (~2.31 Å average), one short Cu-Cl bond (2.2716 Å) are present at the pyramid base, while the apex Cu-Cl bond (2.952 Å) connecting the two metal polyhedra is much longer. In the square planar Cu center two longer Cu-Cl bonds (~2.304 Å average), and two shorter Cu-Cl bonds (~2.268 Å average) are present. One histammonium cation is present for each of the

dianionic chlorometallate tetrahedra, with each cation packing to maximize hydrogen bonding, with a total of 24 hydrogen-bonding interactions within and between each unit cell. The mixed square-pyramidal/square-planar geometry observed in the structure here is not typical of the structures previously observed for $CuCl_4$ based OIHMs, as others have observed a variety of structures dependent mostly on the organic cation identity.[31-33] In one account, a relatively similar structure was found when the dication $(CH_2)_3(NH_3)_2$ was used with $CuCl_4$, which resulted in an additional Cu-Cl bond and a zig-zag square-pyramidal bonding pattern.[34]

The colorless $HistNH_3CdCl_4$ material crystallized from an equimolar mixture of $CdCl_2$ and histammonium dihydrochloride (**Figure 4a**) in a centrosymmetric space group ($P2_1/c$) and exhibited a stacked network of corrugated 2-D structures, with metal octahedra sharing chloride ligands.

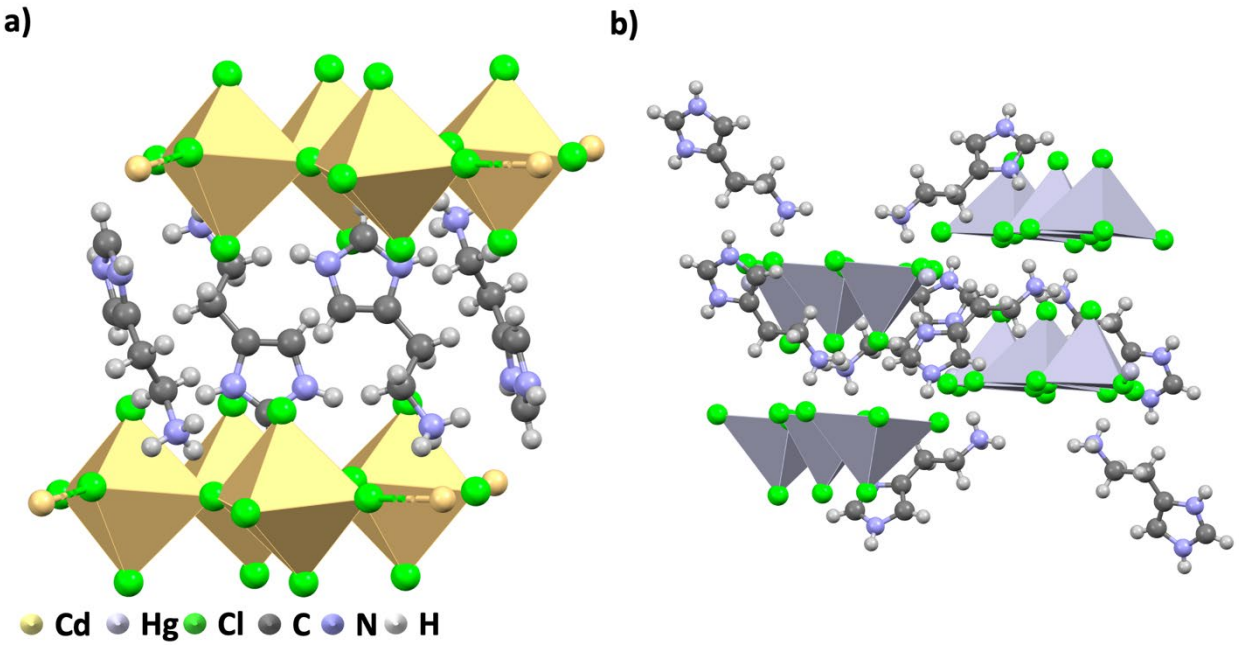

Figure 4. Crystallographically determined X-ray structures of (a) $HistNH_3CdCl_4$ and (b) $HistNH_3HgCl_4$.

Each octahedron is slightly tilted in reference to its neighbors, and in the opposite orientation. Each histammonium dication is oriented head-to-tail with its organic spacer neighbor. In the 2-D sheets, each of the unshared Cl ligands in the plane of the 2-D sheet have a Cd-Cl bond distance of 2.5424 Å, the shared Cl ligands have bond distances of 2.6576 Å and 2.6410 Å, the Cl ligands orthogonal to the 2-D sheet have bond distances of 2.7576 Å and 2.7199 Å. The Cd…Cl…Cd bond angle of one of the shared Cl is 163.11º, the Cl…Cd…Cl angle is 174.53º, while the Cd…Cl…Cd bond angle of the other shared Cl is 179.27º and the Cl…Cd…Cl bond angle is 171.83º. Hydrogen-bonding interactions are present with each of the protonated nitrogens, one each for the imidazolium cations and four for the primary ammonium cations. Since there are four histammonium spacers per unit cell and six hydrogen bond interactions per histammonium, there are 24 hydrogen-bonding interactions within and between each unit cell. The 2-D structure found here is the typical structure found in chlorocadmiates.[35-37]

The colorless $HistNH_3HgCl_4$ material crystallized from an equimolar mixture of $HgCl_2$ and histammonium dihydrochloride (**Figure 4b**) in a centrosymmetric space group (C*2*/c) and exhibited stacked networks of a corrugated 1-D structure, with each of the metals bound to five Cl ligands in a distorted square pyramidal geometry. Two of the Cl basal ligands are shared, two basal Cl ligands unshared, and the apical Cl ligand unshared as well. The apical Hg-Cl bond distance is 2.632 Å, the shared basal Hg-Cl bond distance is 2.4184 Å, the shared Hg…Cl…Hg bond angle is 148.72º and the Cl…Hg…Cl bond angle is 158.57º, and the unshared Hg-Cl bond distance is 2.857 Å with a Cl…Hg…Cl bond angle of 164.34º. Hydrogen-bonding interactions are present with each of the protonated nitrogens, with each imidazolium cation participating in one interaction and four interactions present for the primary ammonium cations. Since there are eight histammonium spacers per unit cell and six hydrogen-bond interactions per histammonium, there

are 48 hydrogen-bonding interactions within and between each unit cell. Others have reported tetrahedral chloromercurate structures,[38-40] but others have observed a similar corrugated 1-D structure from $HgCl_4$.[41]

The colorless $HistNH_3SnCl_4$ material crystallized from an equimolar mixture of $SnCl_2$ and histammonium dihydrochloride (**Figure 5a**) in a centrosymmetric space group (P*21*/c) and exhibited stacked networks of a 0-D structure.

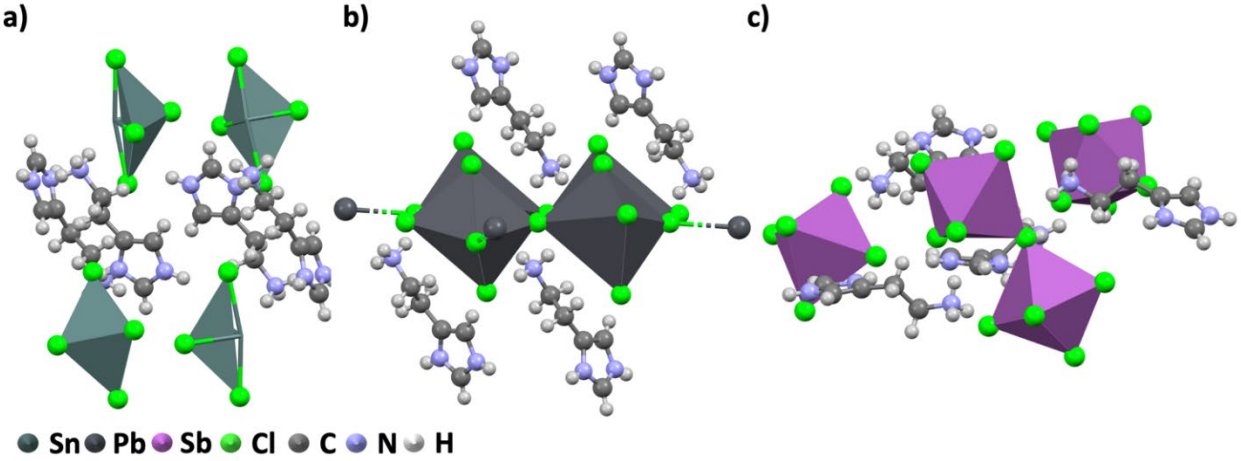

Figure 5. Crystallographically determined X-ray structures of (a) $HistNH_3SnCl_4$, (b) $HistNH_3PbCl_4$, and (c) $HistNH_3SbCl_4$.

Each Sn center is bonded to four Cl ligands in a distorted seesaw geometry, with two shorter Sn-Cl bonds (between 2.5354 and 2.5625 Å), and two longer Sn-Cl bonds (2.7271 and 2.8406 Å). The $Cl_{ax}…Sn…Cl_{ax}$ bond angle was 167.31º, while each of the other Cl...Sn...Cl bond angles was between 84.17 and 87.93º. Three of the Cl ligands participates in hydrogen bonding with the histammonium dication. In each unit cell there are four MCl_4 and four histammonium molecules with a total of five hydrogen bonding interactions per histammonium (three with the ammonium and two with the imidazolium cation), to yield 20 hydrogen-bonding interactions within and between each unit cell. The bond angles observed here for $SnCl_4^{2-}$ are substantially different than those observed in previous studies on 0-D Sn OIHM materials, in which those with

Br and I each exhibited an octahedral geometry.[11] In $SnCl_x$ OIHMs, many others have reported exclusive formation of $[SnCl_6]^{2-}$ octahedra after using $SnCl_2$, which results from Sn^{2+} to Sn^{+4} oxidation, or after using $SnCl_4$.[42-45] In a Cambridge Structural Database search, only one other $SnCl4^{-2}$ with a seesaw geometry was found. [46]

The colorless $HistNH_3PbCl_4$ material crystallized from an equimolar mixture of $PbCl_2$ and histammonium dihydrochloride (**Figure 5b**) in a centrosymmetric space group ($P2_1/c$) and exhibited a stacked network of corrugated 2-D structures, with metal octahedra sharing chloride ligands. Each octahedron is tilted in reference to its neighbors, as in the $HistNH_3CdCl_4$ structure, however, each Pb octahedron is tilted much more, with a Pb-Cl-Pb angle of 150.23º vs. the Pb-Cl-Pb angle of 163.11º. Each histammonium dication is oriented head-to-tail with its organic spacer neighbor, with the ammonium cation in close contact with three Cl ligands. In the 2-D sheets, each of the unshared Cl ligands have Pb-Cl bond distances of 2.7901 and 2.8982 Å, the shared Cl ligands have bond distances of 2.7200 Å and 2.9656 Å, 2.759 Å and 3.0610 Å. The Pb…Cl…Pb bond angle of the one of the shared Cl is 150.23º, the Cl…Pb…Cl angle is 170.78º. Hydrogen-bonding interactions are present with each of the protonated nitrogens, one each for the imidazolium nitrogens and three for the primary ammonium cations. Since there are four histammonium spacers per unit cell and five hydrogen bond interactions per histammonium, there are 20 hydrogen-bonding interactions within and between each unit cell. The 2-D structure observed for $HistNH_3PbCl_4$ was the common n=1 structure, where n is the inorganic layer number, structure reported by others.[47-49]

The colorless $HistNH_3SbCl_5$ material crystallized from an equimolar mixture of $SbCl_3$ and histammonium dihydrochloride (**Figure 5c**) in a non-centrosymmetric space group ($P2_12_12_1$) and exhibited a stacked network of corrugated 1-D structures, with metal octahedra sharing two

chloride ligands. Each octahedron is therefore tilted in reference to its neighbors, each Sb octahedron is tilted away from its neighbor, with a Sb-C_l-Sb angle of 147.98º. Each histammonium dication is oriented head-to-tail with its organic spacer neighbor, with the ammonium cation in close contact with three Cl ligands and the imidazolium in close contact with two Cl ligands. In each octahedron, three Cl ligands have Sb-Cl bond distances between 2.472 and 2.509 Å and one Cl ligand has a bond distance of 2.822 Å. The Sb…Cl bond distance of one of the shared Cl is 2.868 Å., the other is 2.861 Å. Hydrogen-bonding interactions are present with each of the protonated nitrogens, one each for the imidazolium nitrogens and three for the primary ammonium cations. Since there are four histammonium spacers per unit cell and five hydrogen bond interactions per histammonium, there are 20 hydrogen-bonding interactions within and between each unit cell. The corrugated 1-D structure observed for $HistNH_3SbCl_5$ is similar to a recently reported pentachlorantimonate,[50] and to a histammnoium iodoantimonate.[51]

The colorless $(HistNH_3)_3(BiCl_6)_2$ material crystallized from an equimolar mixture of $BiCl_3$ and histammonium dihydrochloride (**Figure 6**) in a centrosymmetric space group (P-*1*) and exhibited stacked networks of a 0-D structure. Also included in the structure are two water and two methanol solvent molecules.

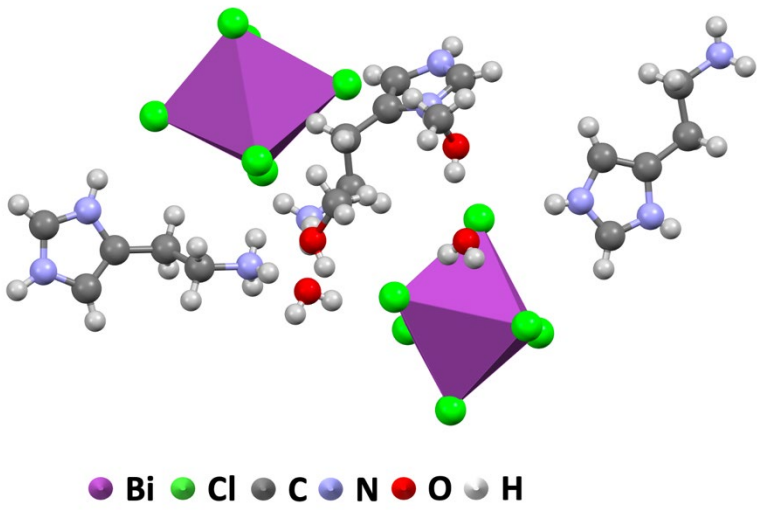

Figure 6. Crystallographically determined X-ray structure of $(HistNH_3)_3(BiCl_6)_2$.

In one of the chlorobismuthates, the Bi center is bonded to six Cl ligands in a distorted octahedron, with two shorter Bi-Cl bonds (2.6512 and 2.6641 Å), two intermediate-length Bi-Cl bonds (2.6925 and 2.7019 Å), and two longer Bi-Cl bonds (2.7556 and 2.7638 Å for example). The Cl_{ax}…Bi…Cl_{ax} bond angle was 174.72º, while each of the other Cl...Bi...Cl bond angles was between 85.68 and 95.74º. In the other chlorobismuthate, the Bi center is also bonded to six Cl ligands in a distorted octahedron, with two shorter Bi-Cl bonds (2.6544 and 2.6824 Å), two intermediate-length Bi-Cl bonds (2.6916 and 2.7032 Å), and two longer Bi-Cl bonds (2.7134 and 2.7781 Å for example). The Cl_{ax}…Bi…Cl_{ax} bond angle was 176.133º, while each of the other Cl...Bi...Cl bond angles was between 84.28 and 95.20º. Each Cl ligand of the two $BiCl_6$ trianions participates in hydrogen bonding, but the types of hydrogen bonds are different between them. In one $BiCl_6$, two chlorine atoms hydrogen bond with nearby water molecules, one chloring atom hydrogen bonds with a nearby methanol molecule, and the other three hydrogen bond with histammine molecules. The water molecules also hydrogen bond to histammine molecules or methanol. In the other $BiCl_6$ group, five of the chlorine atoms hydrogen bond with histammine, but one chlorine is not participating in any hydrogen bonding. In each unit cell there are two MCl_6

and three histammonium molecules. One of the histammines has a total of four hydrogen bonding interactions, one has six, and the other has five. One of the water molecules has three hydrogen bonds and the other has four. One of the methanol molecules has two hydrogen bonds, and the other has three for a total of 27 hydrogen-bonding interactions within and between each unit cell. The bond angles observed here for $BiCl_6^{2-}$ differ from those observed in some previous studies on 0-D Bi OIHM materials, in which the longest Bi-Cl bond lengths here are either longer by <0.05 Å or shorter by >0.13Å than the longest Bi-Cl bond in a $BiCl_6^{3-}$ octahedron.[52-54] Overall, the crystalline structure of the chlorometallate structures described here changed markedly with a change in metal cation identity (**Table 1**).

Table 1. Properties of hybrid inorganic-organic chlorometallates studied here.

Material	Metal Cation Charge	Space Group	Metal Ionic Radius (pm)[55]	Material Dimensionality	Chlorides shared per metal atom
$HistNH_3FeCl_4$	+2	$P2_1/c$	92	0-D	0
$HistNH_3(FeCl_4)_2$	+3	*Pbca*	78.5	0-D	0
$HistNH_3CoCl_4$	+2	$Pna2_1$	88.5	0-D	0
$HistNH_3ZnCl_4$	+2	$Pna2_1$	88	0-D	0
$[HistNH_3Ni(H_2O)Cl_3]Cl$	+2	$P2_1/c$	83	1-D	2
$HistNH_3CuCl_4$	+2	$P2_1/c$	87	0-D dimers	1
$HistNH_3CdCl_4$	+2	$P2_1/c$	109	2-D	4
$HistNH_3HgCl_4$	+2	$C2/c$	116	Corrugated 1-D	1
$HistNH_3SnCl_4$	+2	$P2_1/c$	102[56]	0-D	0

$HistNH_3PbCl_4$	+2	P2_1/c	133	2-D	4
$HistNH_3SbCl5$	+3	P$2_12_12_1$	90	Corrugated 1-D	1
$(HistNH_3)_3(BiCl_6)_2$	+3	P-*1*	117	0-D	0

Most of the materials with a divalent metal cation crystallized into the $P2_1/c$ space group, with the non-centrosymmetric Co- ($Pna2_1$), Zn- ($Pna2_1$), and centrosymmetric Hg-based ((*C2/c)*) materials being the only exceptions. None of the materials exhibited a 3-D dimensionality, where all the chloride ligands are shared with neighboring metal centers. Only two materials (based on Cd and Pb) exhibited a 2-D dimensionality, with four chlorides being shared, and two others (Ni and Hg) exhibited a 1-D dimensionality, with two shared chloride ligands. The histammonium dication is much too large to allow 3-D functionality as determined by the Goldschmidt tolerance factor,[57] and using it resulted in mostly 0-D materials, in metals with varying ionic radii. It is likely that the crystal growth conditions played some role in crystal structure formation (especially for the Ni- and Bi- compounds), which makes precise accounting for the effect of the histammonium cation on dimensionality and space-group more difficult.

While the structures of the materials from **Table 1** depended on the identity of the metal cation, only three of the solved structures were non-centrosymmetric ($HistNH_3CoCl_4$, $HistNH_3ZnCl_4$, and $HistNH_3SbCl_4$). Since we were interested in the potential piezoelectric properties of these chlorometallates, we decided to study further the piezoelectric properties of the non-centrosymmetric materials. The Zn-, Co-, and Sb- based materials were studied, as well as the centrosymmetric $HistNH_3CuCl_4$, which was chosen at random to serve as a negative control. PFM was performed on the X-ray quality Co, Cu, Sb, and Zn containing single-crystal OIHM samples grown and maintained at room temperature. For each of the materials, it was difficult to

consistently see a response displacement from the sample at the applied voltages. We attribute this to difficulties we had in sample mounting, as the crystals were highly brittle and damaged easily,[17] which led to poor electrical contact in some cases. Only the Zn containing material grew large enough crystals in our hands to measure on a specific face (a-c face). **Table 2** shows results of successful PFM measurements from these single-crystal samples. During measurement, only the Zn-containing metallate was stable to testing and storage in ambient atmosphere, which further made PFM testing on the single-crystalline substrates difficult. Nevertheless, when measurements were successfully taken, multiple repetitive sampling events were taken from several sites on the mounted crystal.

Table 2. Local piezoelectric response from piezoresponse force microscopy measurements on unpoled single-crystalline samples of $HistNH_3M^{n+}Cl_{n+2}$ (M=Co, Cu, Zn, Sb) compared to a ferroelectric polymer PVDF reference.[58]

Material	Local Piezoelectric Response (pm/V)
$HistNH_3CoCl_4$	5.17
$HistNH_3CuCl_4$	0.28
$HistNH_3ZnCl_4$	22.6
$HistNH_3SbCl_5$	2.9
PVDF	2.5

To rationalize these results, we performed density functional theory (DFT) calculations using the Perdew-Burke-Ernzerhof (PBE)[59] functional (see Computational details section for more details) for the set of compounds listed in **Table 2**: $HistNH_3CoCl_4$, $HistNH_3SbCl_5$, $HistNH_3CuCl_4$, and $HistNH_3ZnCl_4$.

To compare with the experiment by removing any dependency on the structure, the bandgap, charge transfer, net and cation-Cl dipole moments, and d33 constants provided in **Table 3** were all calculated with PBE at the experimental geometry. Charge transfer and dipole moments were calculated using DDEC6.[60-62]

To examine the variation of the key properties with the different geometries, a comparison of the bandgaps and piezoelectric strain tensors were all calculated with the PBE functional but at four different geometries (see **Tables S9 and S10** of the SI). The four geometries used in this analysis were: (i) experimental; (ii) PBE-partially optimized geometry whereby the volume is fixed but the lattice sites are relaxed; (iii) PBE fully optimized; and (iv) PBE+D3 fully optimized. The comparison between the PBE and PBE+D3 fully optimized geometries were motivated by the fact that the calculated lattice constants and unit-cell volume of the PBE-fully optimized geometries are ca. 10% larger than experiment (see **Table S9**), which is consistent with the previous literature.[63] On the other hand, the lattice constants and unit-cell volume with PBE+D3-optimized geometries are calculated to be within 2% of experiment. Small variations in the band gap energies and piezoelectric strain tensors (**Table S10**) were found depending on the geometry; however, the overall trend is the same.

The PBE-calculated bandgaps at the experimental geometry are in good agreement with the measured values, which were determined using UV-Vis-NIR measurements of dropcasted films (**Table 3**). The observed low energy absorbances in the films of the Co-and Cu- based materials were ascribed to spin-forbidden d-d transitions.[64-67] The piezoelectric strain constants (d_{ij}) were determined from the PBE-calculated elastic (C_{ij}) and piezoelectric stress (e_{ij}) tensors using the relation $d_{ij} = e_{ij} \times S_{ij}$; here, S_{ij} is the inverse of the matrix C_{ij}.[68] As shown in **Table 3**, the calculated d_{33} coefficients for $HistNH_3ZnCl_4$ and $HistNH_3CoCl_4$ are 10.8 pm/V and 7.4 pm/V,

respectively, and 0.0 for $HistNH_3SbCl_4$ and $HistNH_3CuCl_4$ (see Tables S11-S22 for computed tensor components). For $HistNH_3CuCl_4$, the calculated piezoelectric strain coefficients are zero, which is expected because of its centrosymmetric space group ($P2_1/c$). For $HistNH_3SbCl_5$, although the d_{33} value is zero, some of the calculated coefficients are non-zero (**Table S22**). This compares well with the experimental findings that the piezoelectric response is weaker than that for $HistNH_3ZnCl_4$ or $HistNH_3CoCl_4$ (**Table 2**), but much stronger than that for the Cu-containing material because PFM often captures some contributions from non-d_{33} strain tensors (like d_{31} and d_{34}).

The increased experimentally measured piezoelectric responses in going from $HistNH_3SbCl_5$ to $HistNH_3CoCl_4$ and $HistNH_3ZnCl_4$ is attributed to an increase in the cation-Cl bond dipole moment in these compounds (see **Table 3**), which ranges from 0.0 D for $HistNH_3SbCl_5$ to 0.414 D for $HistNH_3CoCl_4$ and 0.479 D for $HistNH_3ZnCl_4$. The overall calculated net dipole moment per unit cell is small because of an apparent cancellation in the contributions from $HistNH_3$ and cation-Cl bond (**Tables S23-S26**). In general, from this analysis, we identify the larger cation-Cl bond dipole to be the source of the larger measured piezoelectric response in $HistNH_3ZnCl_4$ compared with $HistNH_3CoCl_4$.

Table 3. Measured bandgap and calculated bandgap, charge transfer, net dipole moment per unit cell, dipole moment contributed from cation-Cl bond and d_{33} constant in the Co, Sb, Cu, and Zn metalates.

System	Measured bandgap	Calculated bandgap	Charge transfer	Net Dipole moment	Cation-Cl bond Dipole	Calculated d_{33}	Average value of

			(e^-/metal atom)	per unit cell (Debye)	moment (Debye)	constant (pm/V)	*PFM response* (pm/V)
$HistNH_3CoCl_4$	0.88	0.88	0.630	0.037	0.41	7.39	5.17
$HistNH_3SbCl_5$	3.22	2.88	0.957	0.0	0.000	0.00	2.9
$HistNH_3CuCl_4$	0.55	0.53	0.717	0.0	0.000	0.00	0.28
$HistNH_3ZnCl_4$	4.13	4.15	0.635	0.048	0.48	10.76	22.6

To rationalize the larger dipole moment for $HistNH_3ZnCl_4$ compared with $HistNH_3CoCl_4$ and $HistNH_3SbCl_5$, both the elementwise contribution (partial) of the density of states (pDOS) and the projected crystal orbital Hamilton population (pCOHP) were calculated (see Figure 7). The pDOS and pCOHP are used to calculate the contributions of each element to the conduction band minimum (CBM) and valence band maximum (VBM). The COHP analysis was performed using LOBSTER.[69]

Both the pDOS and pCOHP indicates that the higher calculated dipole for $HistNH_3ZnCl_4$, is due to the lower hybridization of the Zn-Cl bond compared with Co-Cl. For $HistNH_3ZnCl_4$, the VBM is dominated by Cl with a slight contribution from Zn and the CBM is dominated by the N atom of $HistNH_3$. Similarly, the COHP analysis indicates that the Zn-Cl bonding dominates the valance band edge but is largely absent from the conduction band edge. This is consistent with experimental data in the literature suggesting that in $ZnCl_4^{2-}$, the electron density of the highest occupied molecular orbital lies mainly in a molecular orbital with primarily Cl ligand *p*-orbital character.[21]

In the isostructural compound $HistNH_3CoCl_4$, the CBM and VBM are both dominated by Co and Cl. This is consistent with the literature that suggests in $CoCl_4^{2-}$, the highest occupied

molecular orbital lies mainly in Co-centered 3d-t_2 orbitals, with little delocalization into the Co-Cl σ bond.[20] In $HistNH_3SbCl_5$ the VBM and CBM is both dominated by Sb and Cl. This agrees with the literature that the valance band is dominated by the strong hybridization between the occupied Sb-5s and Cl-3p while conduction band is dominated by Sb-5p and Cl-3p.[70] Both the VBM and CBM in the case of $HistNH_3CuCl_4$ is dominated by Cu and Cl as suggested by pDOS and COHP analysis.

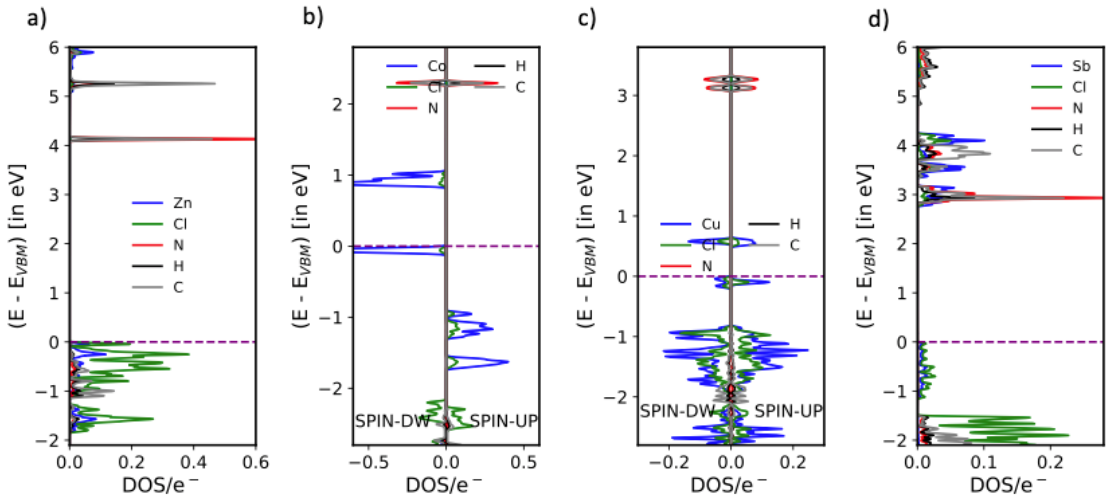

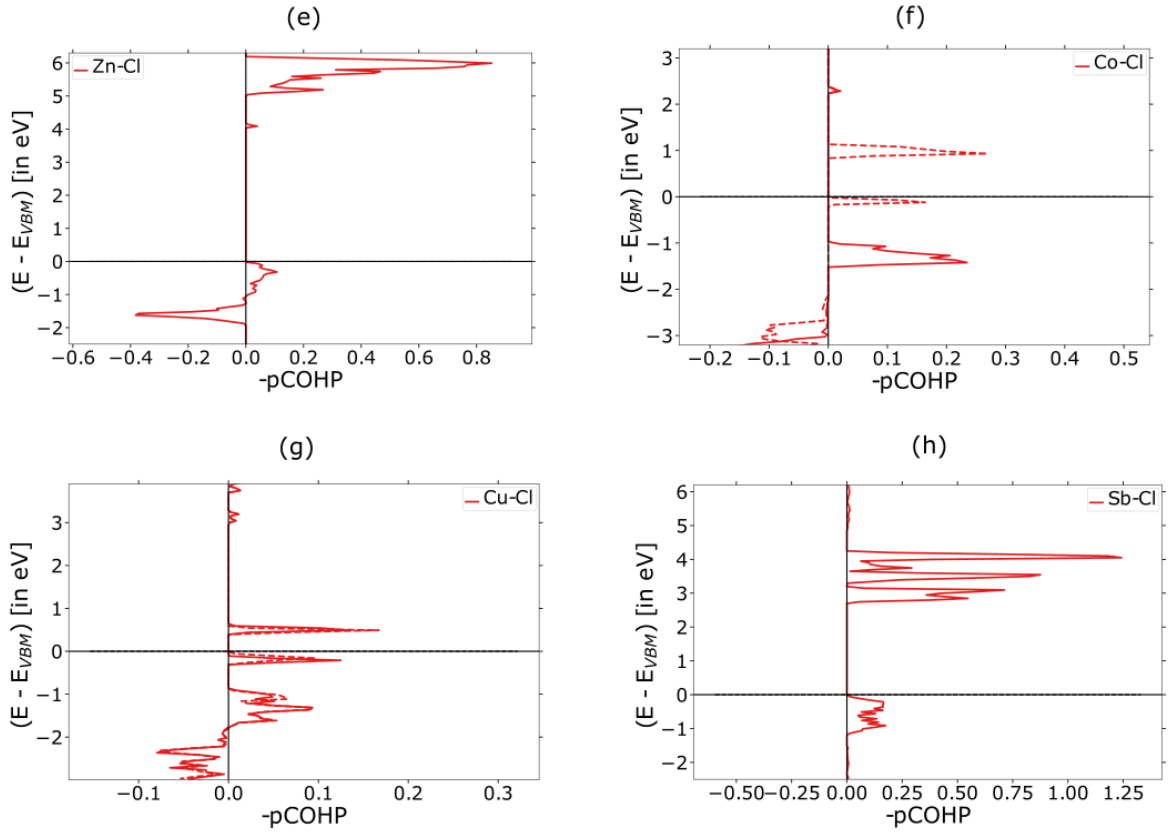

Figure 7. Elementwise contribution on the density of states (DOS) per electrons per atom for (a) $HistNH_3ZnCl_4$, (b) $HistNH_3CoCl_4$, (c) $HistNH_3CuCl_4$, and (d) $HistNH_3SbCl_5$ and projected crystal orbital Hamilton population (pCOHP) of cation-Cl bond in (e) $HistNH_3ZnCl_4$, (f) $HistNH_3CoCl_4$, (g) $HistNH_3CuCl_4$, and (h) $HistNH_3SbCl_5$.

In the results shown in **Table 2**, the $HistNH_3MCl_4$ materials exhibited different local piezoelectric responses compared to the PVDF ferroelectric polymer reference, which was annealed at 100 ºC in an oven and measured according to literature methods.[58] In these trials, the $HistNH_3CuCl_4$ material was the lowest performing overall (0.28 pm/V) and very close to zero, as expected, due to the inversion symmetry present in the crystal. This number is not precisely 0, however, because centrosymmetric materials can give very small local piezoelectric response values.[71] The

$HistNH_3ZnCl_4$ material exhibited the largest average local piezoelectric response, at 22.6 pm/V and $HistNH_3CoCl_4$ yielded a larger local piezoelectric response than PVDF, but much lower than for $HistNH_3ZnCl_4$. $HistNH_3SbCl_5$ exhibited a PFM response that was a little higher than the PVDF reference. The difference in performance between the isostructural Zn and Co based materials is discussed in more detail below. Even though these values are notable, the samples here were tested without any poling treatments, due to difficulty in making electrical connection to the single crystals, thus they are likely underestimated. State-of-the-art approaches towards piezoelectric metallates[72] have yielded materials with d_{33} piezoelectric coefficients of 73 and 76 pm/V for Pb based metallates,[73, 74] 110 pm/V for an Fe based metallate,[75] and 139 and 1540 pm/V for Cd based metallates.[76, 77] While others have suggested that a local inverse piezoelectric response observed from PFM could be extrapolated into a bulk d_{33} value,[78] which would place $HistNH_3ZnCl_4$ firmly within the state-of-the-art, we were not able to pole these samples as of yet. Efforts are underway to grow sufficiently large crystals to allow poling and bulk d_{33} piezoelectric measurement.

To further investigate whether the piezoelectric response measurements are related to orientation of the mounted single crystals, $HistNH_3MCl_4$ (M = Cu, Co, Zn)·PVDF composite materials were made by drop-casting, annealing in an oven, and peeling composite films post-anneal to yield a free standing and flexible film. The metallate to PVDF ratio, annealing temperatures, and times were optimized by choosing the compositions and temperatures that led to the easiest-to-peel and handle films after fabrication. The easily handled and non-poled films were then tested by PFM.[6] For $HistNH_3ZnCl_4$·PVDF the composite was 8.6 wt.% $HistNH_3ZnCl_4$ which was annealed at 100 ºC for 15 minutes, for $HistNH_3CuCl_4$·PVDF the composite was 5.1 wt.% $HistNH_3CuCl_4$ which was annealed at 150 ºC for 15 minutes, and for $HistNH_3CoCl_4$·PVDF the composite was 5.1 wt.% $HistNH_3CoCl_4$ which was annealed at 180 ºC for 15 minutes. Of the composite materials, the

$HistNH_3ZnCl_4$·PVDF composite films at 8.6 wt.% were more resistant to water-induced film degradation than the other composites, which required storage in dry air after fabrication. In addition, the $HistNH_3CuCl_4$·PVDF and $HistNH_3CoCl_4$·PVDF composites with higher than 5.1 wt.% metallate was not easily peeled and were therefore not chosen for further testing. Attempts to make the Sb-containing composites did not yield easily peeled films in our attempts. PXRD measurements of the films indicated similar diffractions for the Zn-based composite and single crystal, but the Co-based composite had no discernable diffraction besides PVDF and the Cu-based composite did not exhibit diffraction peaks that were similar to those simulated from the crystal. Therefore, it is possible that only the Zn-based composite contained the same metallate structure as was solved by powder X-ray diffraction. The 60 x 60 μm topography images shown in the insets of **Figure 8** were taken using contact mode at a scan rate of 0.1 Hz. A linear regression analysis was carried out for each measurement. The slope of the voltage vs displacement was taken to obtain the local piezoelectric response (see *Supporting Information*). **Figure 8** reports the average of the slopes from the 10 different measurements and their standard deviation. To remove the background noise from the measurements, a single measurement was performed on a non-piezoelectric sample (a glass slide) using the same parameters. The measured response of the non-piezoelectric sample was subtracted out of the signals from the polymer composites.

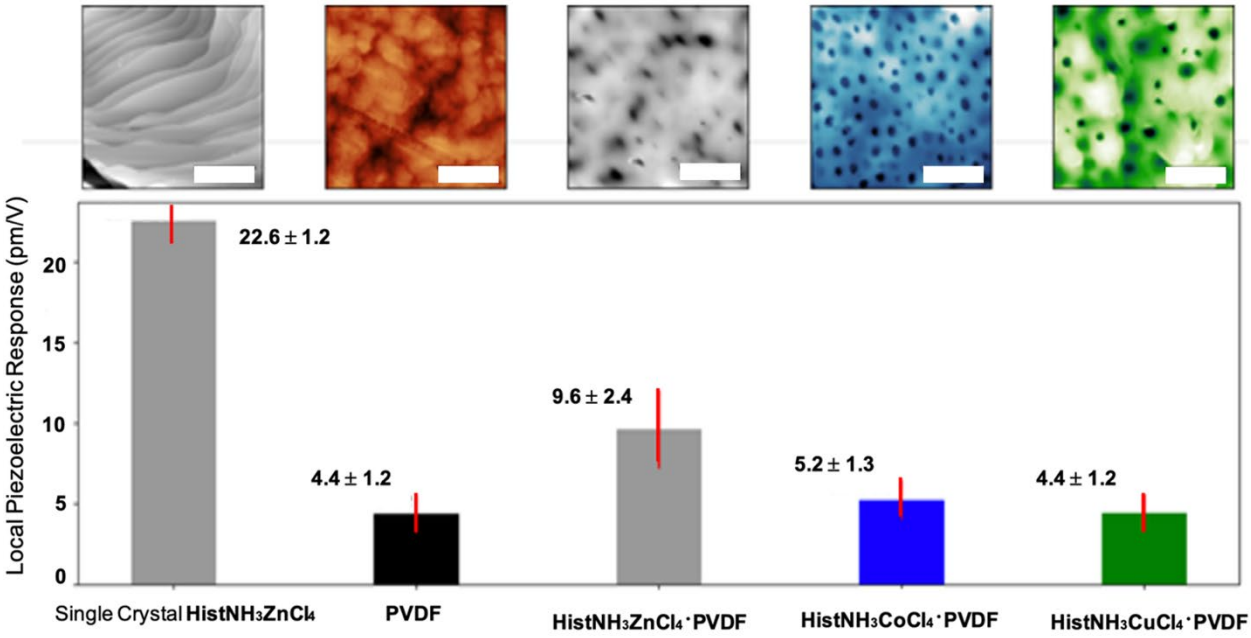

Figure 8. Shown above are the average local piezoelectric responses for all three polymer composite samples without poling, compared with a reference PVDF polymer sample and a single-crystal $HistNH_3ZnCl_4$ sample. Above each sample is a 60 x 60 μm topography image of each material, taken using contact mode at a scan rate of 0.1 Hz, with a scale bar of 20 μm. Listed from left to right are the $HistNH_3ZnCl_4$ (single crystal), PVDF reference film, $HistNH_3ZnCl_4$·PVDF composite, $HistNH_3CoCl_4$·PVDF composite and $HistNH_3CuCl_4$·PVDF composite.

From the PFM measurements on the polymer/metallate composite materials, a similar trend to that observed with single-crystal samples was observed. The $HistNH_3ZnCl_4$·PVDF composite yielded the highest local piezoelectric response (9.6 ± 2.4 pm/V), and the $HistNH_3CoCl_4$·PVDF yielded a response marginally better response than the reference PVDF film (5.2 ± 1.3 pm/V). The $HistNH_3CuCl_4$·PVDF composite yielded no improvement over the unmodified PVDF films (4.4 ± 1.2 pm/V), as would be expected for a non-piezoelectric material. The piezoelectric longitudinal d_{33} charge coefficients using the Berlincourt method of all the composite samples can be seen in

Table S8. The magnitude of the d_{33} coefficients measured via the Berlincourt method are relatively small compared to the PFM data in **Table 2**, with values of 0.31 pm/V for $HistNH_3ZnCl_4$•PVDF, 0.24 pm/V for $HistNH_3CoCl_4$•PVDF, and 0.09 pm/V for $HistNH_3CuCl_4$•PVDF. We attribute this due to differences between the Berlincourt piezo-meter, which is a bulk measurement of the metallate composite using upper and lower electrodes, and PFM which is a localized surface measurement that brings a sharp conductive probe into contact with the metallate composite surface. Since PFM is a localized surface measurement, it is less influenced by the polymer phase and therefore tends to exhibit high d_{33} values, while the Berlincourt piezo-meter operates through thickness mode, and the polarization and measured d_{33} coefficient is dominated by the continuous polymer phase.

To further confirm that each material was noncentrosymmetric at temperatures similar to those used in PFM measurement, we undertook optical second-harmonic generation (SHG) studies. This is a common way to screen for ferroelectrics because SHG only occurs in materials that lack inversion symmetry.[79] We used a Zeiss LSM880 upright multiphoton microscope with tunable laser power, excitation wavelength and detection wavelength (**Figure 9**). We were unsuccessful in making crystalline powders with specific particle sizes, so we turned to using single crystals for our measurements. X-ray quality single crystals were used to verify material identity and then they were sliced with a razor blade to reduce surface irregularities and mounted with an arbitrary crystallographic orientation. We compared the values we found to samples of poled PVDF sheets and a large single crystalline potassium dihydrogen phosphate (KDP) sample, both of which are typical piezoelectric reference materials.

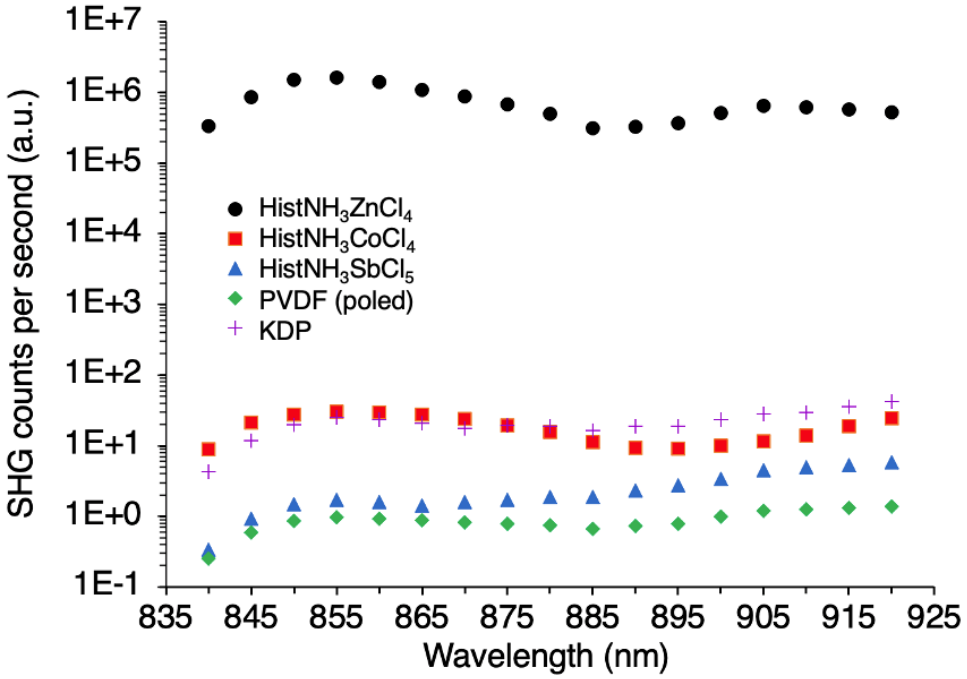

Figure 9. Second Harmonic Generation activity for single crystals of $HistNH_3ZnCl_4$ (black circles), $HistNH_3CoCl_4$ (red squares), and $HistNH_3SbCl_5$ (blue triangles), a sheet of poled PVDF (green diamonds), and single crystals of KDP (purple crosses). The incidence of light has been normalized for each of the samples.

We scanned excitation wavelengths from 920 – 840 nm and observed the intensity of λ/2 emission. During the measurement, we found that each of the Zn-, Co-, and Sb-containing materials produced λ/2 light. For samples with an inversion center, no light was observed. For the two reference materials, the poled PVDF and KDP samples both exhibited a SHG response as well. These data confirm that each of the chlorometallate materials are non-centrosymmetric as grown and as measured by PFM, and not only at the low temperature in which their structures were solved by X-ray crystallography. Because sample thickness, light scattering, absorption, and surface irregularities can play a large role in the magnitude of SHG response measured,[80] these

SHG measurement values are not meant to be quantitative. Until powders of each material with specific particle sizes can be reliably formed, then these figures cannot be presented quantitatively.

Conclusions

In conclusion, we have synthesized a range of novel organic-inorganic hybrid chlorometallates, including three systems that crystallized in a non-centrosymmetric space group. We determined that using different metal B site cations, a range of metallate dimensionality, symmetry, and degree of halide sharing could be accessed when using the histammonium dication. We evaluated the local piezoelectric response of the three materials using piezoresponse force microscopy, $HistNH_3ZnCl_4$, $HistNH_3CoCl_4$, $HistNH_3SbCl_5$ and found that even though they are isostructural, the Zn containing material exhibited a much higher response than the Co containing material. We verified that each non-centrosymmetric structure retained its low-symmetry structure at room temperature using second harmonic generation spectroscopy. We then correlated the piezoelectric response difference of the Co and Zn materials to material properties. It was found that the $ZnCl_4$ containing material exhibited a higher piezoelectric response than $CoCl_4$ in crystal and composite form, which was attributed to a higher material dipole moment, larger strain tensors, and a much wider bandgap for the $ZnCl_4$ material than for the $CoCl_4$ material. This study provides new insights on the impact of B site cation choice on material piezoelectric and structural properties of the material.

Experimental

General Considerations: Reagents used as received from the following chemical suppliers: hydrochloric acid and histamine dihydrochloride were purchased from Matrix Scientific and the transition metal chlorides from various sources. Differential scanning calorimetry measurements were acquired on a TA-Instruments TRIOS DSC 2500 from 0 to 200 °C.

Materials and Solutions Preparation

The various histammonium HOIP single crystals were grown by dissolving the transition metal halides $M^{x+}Cl_x$ (M= Fe^{2+}, Fe^{3+}, Cu^{2+}, Co^{2+}, Ni^{2+}, Zn^{2+}, Cd^{2+}, Hg^{2+}, Sn^{2+}, Pb^{2+}, Sb^{3+}, Bi^{3+}) (1.0 mmol) and histammonium dihydrochloride in either 1 mL of hydrochloric acid, 1 mL of water acidified to pH 3 with HCl, 1 mL of 1:1 methanol:water acidified to pH = 3, or 1 mL of DMSO in a capped 2 mL vial,. In each case, the contents were warmed until dissolution before being left to crystallize. The single-crystal samples were left to grow over the course of several days.

Metallate Composite Film Preparation

Composite films used for PFM measurements were prepared by dissolving PVDF (10 wt%) and histammoniumMCl_4 (M = Co, Cu, Zn), drop-casting 50 μL of the solution onto a soda lime glass slide, and then annealed in an oven.

Single-Crystal Characterization

Single-crystal data of the metallates collected on a Bruker D8 Venture κ-axis diffractometer with Mo Kα radiation (0.71073 Å) at 90.0 K. The crystal structures were solved by dual-space methods and refined by full-matrix least-squares using the SHELX programs.[81]

PFM Characterization

Each sample was mounted onto a polished aluminum puck using carbon sticky tape as a conductive adhesive. Piezoresponse force microscopy (PFM) was performed on all samples as well as a poly(vinylidene difluoride) (PVDF) reference sample at 10 different locations using a Bruker Dimension Icon mounted with a SCM-PIT-V2 platinum-iridium coated conductive tip. To determine the measured displacement of the surface, the tip was calibrated using fused silica to determine the deflection sensitivity. A thermal tuning procedure was also performed to determine the quality factor of the tip (Q = 184). A single measurement at a location consisted of measuring the displacement of the sample when applying 0, 2, 4, 6, 8, and 10 V by scanning a 500 x 167 nm^2 area at an applied load of 68 nN. At each voltage, the response of the sample was taken to be the average response of the resulting image (averaging over ~22,000 data points).

Piezoelectric charge coefficients, d_{33}, of all samples with top and bottom electrodes were measured before and after corona poling by the Berlincourt method in a higher precision mode of piezo-meter (PiezoTest PM300, Singapore). For each sample, three measurements in both positive and negative d_{33} were taken before and after corona poling to evaluate the piezoelectric response of all samples.

Second Harmonic Generation Measurement

X-ray quality single crystals of Co, Sb, Zn were first sliced with a razorblade and the sliced crystal mounted on a soda lime glass slide with arbitrary crystallographic orientation. The slide was then mounted into a Zeiss LSM880 upright multiphoton microscope and illuminated with light between 840 nm and 920 at a 5x lens objective. The emitted light matching λ/2 nm is detected for all in-focus light and plotted versus the wavelength.

Experimental Bandgap Determination

Thin films of Cu, Co, Sb, and Zn OIHMs formed by drop casting 1M precursor solutions onto sodalime glass microscope slides, annealing at 100 ºC for 5 min and recording the transmission spectra of the thick, polycrystalline film using a Cary5000 UV/Vis/NIR spectrophotometer.

Computational details

All DFT calculations were performed using the Vienna ab initio simulation package (VASP) code by utilizing the Perdew-Burke-Ernzerhof (PBE)[59] exchange-correlation functional and the pseudopotentials recommended by VASP. Gaussian smearing with smearing parameter (K_BT) of 0.02 eV, energy convergence criterion for the electronic steps equal to 10^{-7} eV and the gamma-centered k-meshes with the smallest allowed spacing between k-points equal to 0.03 $Å^{-1}$ for the Brillouin zone sampling was used in all the calculations. In addition, the calculations of Cu- and Co-based materials were initialized in three different spin configurations (ferromagnetic, ferrimagnetic, and anti-ferromagnetic). However, the subsequent analyses were performed only on the structure corresponding to the minimum energy. For Cu- and Co-based materials we found the minimum energy corresponding to antiferromagnetic and ferromagnetic spin configuration, respectively. We also computed the elastic tensor following the strain-stress relationship[82] and the piezoelectric stress tensor[83, 84] using the linear response theory as described in the literature. Finally, we utilized the Density Derived Electrostatic and Chemical (DDEC6)[60-62] approach to obtain the net atomic charges and dipole moment on each atom in the calculated structure. LOBSTER package[69] version 4.1.0 was utilized for the chemical-bonding interaction using the "pbevaspfit2015" basis set. The necessary static self-consistent calculations were performed by switching off the symmetry as suggested in the LOBSTER manual.

Supporting Information

The Supporting Information is available free of charge at https://pubs.acs.org/. Additional experimental and theoretical details and materials and methods, including tables and figures.

Accession Codes

CCDC 2202659-2202670 contain the supplementary crystallographic data for this paper. These data can be obtained free of charge via www.ccdc.cam.ac.uk/data_request/cif, or by emailing data_request@ccdc.cam.ac.uk, or by contacting The Cambridge Crystallographic Data Centre, 12 Union Road, Cambridge CB2 1EZ, UK; fax: +44 1223 336033.

Acknowledgments

We thank Prof. Y.T. Cheng for access to PFM instrumentation. C.S. and S.A. acknowledge support from the University of South Carolina and AFOSR (20IOE044). A.H. acknowledges startup funds from the University of Kentucky, D.A. acknowledges REU funding (NSF 1757354). This material is based upon work supported by the National Science Foundation under Cooperative Agreement No. 1849213.

References

1. Kojima, A.; Teshima, K.; Shirai, Y.; Miyasaka, T., Organometal Halide Perovskites as Visible-Light Sensitizers for Photovoltaic Cells. *Journal of the American Chemical Society* **2009,** *131* (17), 6050-6051.https://doi.org/10.1021/ja809598r

2. Tan, Z.-K.; Moghaddam, R. S.; Lai, M. L.; Docampo, P.; Higler, R.; Deschler, F.; Price, M.; Sadhanala, A.; Pazos, L. M.; Credgington, D.; Hanusch, F.; Bein, T.; Snaith, H. J.; Friend, R. H., Bright

Light-Emitting Diodes Based on Organometal Halide Perovskite. *Nature Nanotechnology* **2014,** *9* (9), 687-692.https://doi.org/10.1038/nnano.2014.149
3. Xing, G.; Mathews, N.; Lim, S. S.; Yantara, N.; Liu, X.; Sabba, D.; Grätzel, M.; Mhaisalkar, S.; Sum, T. C., Low-Temperature Solution-Processed Wavelength-Tunable Perovskites for Lasing. *Nature Materials* **2014,** *13* (5), 476-480.https://doi.org/10.1038/nmat3911
4. Fang, Y.; Dong, Q.; Shao, Y.; Yuan, Y.; Huang, J., Highly Narrowband Perovskite Single-Crystal Photodetectors Enabled by Surface-Charge Recombination. *Nature Photonics* **2015,** *9* (10), 679-686.https://doi.org/10.1038/nphoton.2015.156
5. Park, N.-G., Crystal Growth Engineering for High Efficiency Perovskite Solar Cells. *CrystEngComm* **2016,** *18* (32), 5977-5985.http://dx.doi.org/10.1039/C6CE00813E
6. Wang, M.; Feng, Y.; Bian, J.; Liu, H.; Shi, Y., A Comparative Study of One-Step and Two-Step Approaches for Mapbi3 Perovskite Layer and Its Influence on the Performance of Mesoscopic Perovskite Solar Cell. *Chemical Physics Letters* **2018,** *692*, 44-49.
7. Jin, S., Can We Find the Perfect a-Cations for Halide Perovskites? *ACS Energy Letters* **2021,** *6* (9), 3386-3389.https://doi.org/10.1021/acsenergylett.1c01806
8. Lin, H.; Zhou, C.; Tian, Y.; Siegrist, T.; Ma, B., Low-Dimensional Organometal Halide Perovskites. *ACS Energy Letters* **2018,** *3* (1), 54-62.https://doi.org/10.1021/acsenergylett.7b00926
9. Zhou, C.; Lee, S.; Lin, H.; Neu, J.; Chaaban, M.; Xu, L.-J.; Arcidiacono, A.; He, Q.; Worku, M.; Ledbetter, L.; Lin, X.; Schlueter, J. A.; Siegrist, T.; Ma, B., Bulk Assembly of Multicomponent Zero-Dimensional Metal Halides with Dual Emission. *ACS Materials Letters* **2020,** *2* (4), 376-380.
10. Lin, H.; Zhou, C.; Neu, J.; Zhou, Y.; Han, D.; Chen, S.; Worku, M.; Chaaban, M.; Lee, S.; Berkwits, E.; Siegrist, T.; Du, M. H.; Ma, B., Bulk Assembly of Corrugated 1d Metal Halides with Broadband Yellow Emission. *Advanced Optical Materials* **2019,** *7* (6).
11. Zhou, C.; Lin, H.; Tian, Y.; Yuan, Z.; Clark, R.; Chen, B.; van de Burgt, L. J.; Wang, J. C.; Zhou, Y.; Hanson, K.; Meisner, Q. J.; Neu, J.; Besara, T.; Siegrist, T.; Lambers, E.; Djurovich, P.; Ma, B., Luminescent Zero-Dimensional Organic Metal Halide Hybrids with near-Unity Quantum Efficiency. *Chem Sci* **2018,** *9* (3), 586-593.https://www.ncbi.nlm.nih.gov/pubmed/29629122
12. Akkerman, Q. A.; Manna, L., What Defines a Halide Perovskite? *ACS Energy Letters* **2020,** *5* (2), 604-610.https://doi.org/10.1021/acsenergylett.0c00039
13. Lauher, J. W.; Ibers, J. A., Structure of Tetramethylammonium Tetrachloroferrate(Ii). Comparison of Iron(Ii) and Iron(Iii) Bond Lengths in High-Spin Tetrahedral Environments. *Inorganic Chemistry* **1975,** *14* (2), 348-352.https://doi.org/10.1021/ic50144a029
14. Richards, R. R.; Gregory, N. W., The Crystal Structure of Sodium Tetrachloroferrate(Iii). *The Journal of Physical Chemistry* **1965,** *69* (1), 239-244.https://doi.org/10.1021/j100885a035
15. Kistenmacher, T. J.; Stucky, G. D., Structural and Spectroscopic Studies of Tetrachlorophosphonium Tetrachloroferrate(Iii), [Pcl4][Fecl4]. *Inorganic Chemistry* **1968,** *7* (10), 2150-2155.https://doi.org/10.1021/ic50068a040
16. Mason, R.; McKenzie, E. D.; Robertson, G. B.; Rusholme, G. A., Thioacetylacetone Complexes of Iron(Ii). *Chemical Communications (London)* **1968,** (24), 1673-1674.http://dx.doi.org/10.1039/C19680001673
17. Hempel, J. L.; Wells, M. D.; Parkin, S.; Cheng, Y.-T.; Huckaba, A. J., Unveiling the Brittleness of Hybrid Organic–Inorganic 0-D Histammonium Zinc Chlorometallate by Nanoindentation. *Applied Physics Letters* **2021,** *119* (24), 241903.https://aip.scitation.org/doi/abs/10.1063/5.0064031
18. Cole, L. B.; Holt, E. M., Structure of (Histamine.2h+)(Zncl4). *Acta Crystallographica Section C* **1990,** *46* (9), 1737-1739.https://doi.org/10.1107/S0108270190002773
19. Bonnet, J. J.; Jeannin, Y. Y., Etude Cristallographique De Tetrachlorocobaltate(Ii) D'histamine Diprotonee. *Acta Crystallographica Section B* **1972,** *28* (4), 1079-1085.https://doi.org/10.1107/S0567740872003759

20. Figgis, B. N.; Reynolds, P. A.; White, A. H., Charge Density in the Cocl42– Ion: A Comparison with Spin Density and Theoretical Calculations. *Journal of the Chemical Society, Dalton Transactions* **1987,** (7), 1737-1745.http://dx.doi.org/10.1039/DT9870001737
21. Clarke, C. J.; Hayama, S.; Hawes, A.; Hallett, J. P.; Chamberlain, T. W.; Lovelock, K. R. J.; Besley, N. A., Zinc 1s Valence-to-Core X-Ray Emission Spectroscopy of Halozincate Complexes. *The Journal of Physical Chemistry A* **2019,** *123* (44), 9552-9559.https://doi.org/10.1021/acs.jpca.9b08037
22. Zhang, X.; Li, L.; Wang, S.; Liu, X.; Yao, Y.; Peng, Y.; Hong, M.; Luo, J., [(N-Aepz)Zncl4]Cl: A "Green" Metal Halide Showing Highly Efficient Bluish-White-Light Emission. *Inorganic Chemistry* **2020,** *59* (6), 3527-3531.https://doi.org/10.1021/acs.inorgchem.0c00078
23. Chen, M.; Su, C.-Y.; Zhang, W.-Y.; Wang, W.-Y.; Huang, P.-Z.; Zhang, Y.; Fu, D.-W., Organic-Inorganic Hybrid Crystal [1-Methylpiperidinium]2[Zncl4] with High Tc Phase Transition and Dielectric Switches. *European Journal of Inorganic Chemistry* **2021,** *2021* (41), 4307-4313.https://chemistry-europe.onlinelibrary.wiley.com/doi/abs/10.1002/ejic.202100671
24. Decaroli, C.; Arevalo-Lopez, A. M.; Woodall, C. H.; Rodriguez, E. E.; Attfield, J. P.; Parker, S. F.; Stock, C., (C4h12n2)[Cocl4]: Tetrahedrally Coordinated Co2+ without the Orbital Degeneracy. *Acta Crystallographica Section B* **2015,** *71* (1), 20-24.https://doi.org/10.1107/S2052520614024809
25. Parkin, S., Practical Hints and Tips for Solution of Pseudo-Merohedric Twins: Three Case Studies. *Acta Crystallographica Section E* **2021,** *77* (5), 452-465.https://doi.org/10.1107/S205698902100342X
26. Gerdes, A.; Bond, M. R., Octakis(Dimethylammonium) Hexa-[Mu]2-Chlorido-Hexachloridotrinickelate(Ii) Dichloride: A Linear Trinickel Complex with Asymmetric Bridging. *Acta Crystallographica Section C* **2009,** *65* (10), m398-m400.https://doi.org/10.1107/S0108270109036853
27. Ben Salah, A. M.; Walha, S.; Yahyaoui, S.; Abdalrahman, M.; Turnbull, M. M.; Mhiri, T.; Naïli, H., Crystal Growth, Thermal and Magnetic Characterizations of a New Ferromagnetic Ni(Ii) Dimer. *Monatshefte für Chemie - Chemical Monthly* **2014,** *145* (10), 1575-1581.https://doi.org/10.1007/s00706-014-1230-9
28. Gill, N. S.; Nyholm, R. S., 802. Complex Halides of the Transition Metals. Part I. Tetrahedral Nickel Complexes. *Journal of the Chemical Society (Resumed)* **1959,** (0), 3997-4007.http://dx.doi.org/10.1039/JR9590003997
29. Meredith, M. B.; McMillen, C. H.; Goodman, J. T.; Hanusa, T. P., Ambient Temperature Imidazolium-Based Ionic Liquids with Tetrachloronickelate(Ii) Anions. *Polyhedron* **2009,** *28* (12), 2355-2358.https://www.sciencedirect.com/science/article/pii/S0277538709002472
30. Cotton, F. A.; Faut, O. D.; Goodgame, D. M. L., Preparation, Spectra and Electronic Structures of Tetrahedral Nickel(Ii) Complexes Containing Triphenylphosphine and Halide Ions as Ligands. *Journal of the American Chemical Society* **1961,** *83* (2), 344-351.https://doi.org/10.1021/ja01463a021
31. Arramel, A.; Fauzi, A. D.; Yin, X.; Tang, C. S.; Mahyuddin, M. H.; Sahdan, M. F.; Aminah, M.; Onggo, D.; Shukri, G.; Diao, C.; Wang, H.; Birowosuto, M. D.; Wee, A. T. S.; Rusydi, A., Ligand Size Effects in Two-Dimensional Hybrid Copper Halide Perovskites Crystals. *Communications Materials* **2021,** *2* (1), 70.https://doi.org/10.1038/s43246-021-00175-6
32. Li, Q.; Li, S.; Wang, K.; Quan, Z.; Meng, Y.; Zou, B., High-Pressure Study of Perovskite-Like Organometal Halide: Band-Gap Narrowing and Structural Evolution of [Nh3-(Ch2)4-Nh3]Cucl4. *The Journal of Physical Chemistry Letters* **2017,** *8* (2), 500-506.https://doi.org/10.1021/acs.jpclett.6b02786
33. Abdel-Aal, S. K.; Kandeel, M. F.; El-Sherif, A. F.; Abdel-Rahman, A. S., Synthesis, Characterization, and Optical Properties of New Organic–Inorganic Hybrid Perovskites [(Nh3)2(Ch2)3]Cucl4 and [(Nh3)2(Ch2)4]Cucl2br2. *physica status solidi (a)* **2021,** *218* (12), 2100036.https://onlinelibrary.wiley.com/doi/abs/10.1002/pssa.202100036
34. Lim, A. R., Structural Characterization, Thermal Properties, and Molecular Motions near the Phase Transition in Hybrid Perovskite [(Ch2)3(Nh3)2]Cucl4 Crystals: 1h, 13c, and 14n Nuclear Magnetic Resonance. *Scientific Reports* **2020,** *10* (1), 20853.https://doi.org/10.1038/s41598-020-77931-0

35. Lim, A. R.; Kim, S. H., Physicochemical Property Investigations of Perovskite-Type Layer Crystals [Nh3(Ch2)Nnh3]Cdcl4 (N = 2, 3, and 4) as a Function of Length N of Ch2. *ACS Omega* **2021,** *6* (41), 27568-27577.https://doi.org/10.1021/acsomega.1c04671
36. Sui Li, L.; Juan Wei, W.; Qiang Gao, H.; Hui Tan, Y.; Bo Han, X., Molecular Disorder Induces an Unusual Phase Transition in a Potential 2d Chiral Ferroelectric Perovskite. *Chemistry – A European Journal* **2021,** *27* (35), 9054-9059.https://chemistry-europe.onlinelibrary.wiley.com/doi/abs/10.1002/chem.202100334
37. Costin-Hogan, C. E.; Chen, C.-L.; Hughes, E.; Pickett, A.; Valencia, R.; Rath, N. P.; Beatty, A. M., "Reverse" Engineering: Toward 0-D Cadmium Halide Clusters. *CrystEngComm* **2008,** *10* (12), 1910-1915.http://dx.doi.org/10.1039/B812504J
38. Belhouchet, M.; Wamani, W.; Mhiri, T., Synthesis, Structure and Spectroscopic Investigations of Two New Organic-Inorganic Hybrids Nh3(C6h4)2nh3cucl4and Nh3(C6h4)2nh3hgcl4. *IOP Conference Series: Materials Science and Engineering* **2010,** *13*, 012039.http://dx.doi.org/10.1088/1757-899X/13/1/012039
39. Asahi, T.; Hasebe, K.; Gesi, K., A Structural Study of [N(Ch3)4]2hgcl4 in Connection with Its Phase Transition. *Journal of the Physical Society of Japan* **1991,** *60* (3), 921-926.https://doi.org/10.1143/JPSJ.60.921
40. Vezzosi, I. M.; Benedetti, A.; Albinati, A.; Ganazzoli, F.; Cariati, F.; Pellicciari, L., Spectroscopic and Structural Investigation on Tetrahalomercurates(Ii). Crystal and Molecular Structures of Bis(N-Ethylmorpholinium)Tetrachloromercurate(Ii) and (N-Ammoniumethylmorpholinium)Tetrachloromercurate(Ii) Complexes. *Inorganica Chimica Acta* **1984,** *90* (1), 1-7.https://www.sciencedirect.com/science/article/pii/S0020169300807124
41. Wang, W.; Wen, W.-F.; Liu, C.-S.; He, L.-F.; Zhang, Y.; Yang, S.-L.; Chen, W.-T., Syntheses, Structures, Solid-State Photoluminescence and Optical Band Gaps of Two Novel Heterometallic Lanthanide/Mercury Compounds. *Journal of Solid State Chemistry* **2020,** *291*, 121623.https://www.sciencedirect.com/science/article/pii/S0022459620304539
42. Feddaoui, I.; Abdelbaky, M. S. M.; García-Granda, S.; Essalah, K.; Ben Nasr, C.; Mrad, M. L., Synthesis, Crystal Structure, Vibrational Spectroscopy, Dft, Optical Study and Thermal Analysis of a New Stannate(Iv) Complex Based on 2-Ethyl-6-Methylanilinium (C9h14n)2[Sncl6]. *Journal of Molecular Structure* **2019,** *1186*, 31-38.https://www.sciencedirect.com/science/article/pii/S0022286019302613
43. Knop, O.; Cameron, T. S.; James, M. A.; Falk, M., Bis(Triethylammonium) Hexachlorostannate (Iv): Crystal Structure and Hydrogen Bonding. *Canadian Journal of Chemistry* **1981,** *59* (16), 2550-2555.https://doi.org/10.1139/v81-367
44. Ines, M.; Gzaiel, M. B.; Oueslati, A.; Auguste, S.; Lhoste, J.; Gargouri, M., Crystal Structure and Electrical Conduction Mechanism of the New Bi-Tetrabutylphosphonium Hexachlorostannate Compound. *Journal of Molecular Structure* **2021,** *1226*, 129361.https://www.sciencedirect.com/science/article/pii/S0022286020316793
45. Pisanu, A.; Coduri, M.; Morana, M.; Ciftci, Y. O.; Rizzo, A.; Listorti, A.; Gaboardi, M.; Bindi, L.; Queloz, V. I. E.; Milanese, C.; Grancini, G.; Malavasi, L., Exploring the Role of Halide Mixing in Lead-Free Bza2snx4 Two Dimensional Hybrid Perovskites. *Journal of Materials Chemistry A* **2020,** *8* (4), 1875-1886.http://dx.doi.org/10.1039/C9TA11923J
46. Zhong, C.; Sasaki, T.; Jimbo-Kobayashi, A.; Fujiwara, E.; Kobayashi, A.; Tada, M.; Iwasawa, Y., Syntheses, Structures, and Properties of a Series of Metal Ion-Containing Dialkylimidazolium Ionic Liquids. *Bulletin of the Chemical Society of Japan* **2007,** *80* (12), 2365-2374.https://doi.org/10.1246/bcsj.80.2365
47. Du, K.-z.; Tu, Q.; Zhang, X.; Han, Q.; Liu, J.; Zauscher, S.; Mitzi, D. B., Two-Dimensional Lead(Ii) Halide-Based Hybrid Perovskites Templated by Acene Alkylamines: Crystal Structures, Optical Properties,

and Piezoelectricity. *Inorganic Chemistry* **2017,** *56* (15), 9291-9302.https://doi.org/10.1021/acs.inorgchem.7b01094
48. Li, X.; Hoffman, J. M.; Kanatzidis, M. G., The 2d Halide Perovskite Rulebook: How the Spacer Influences Everything from the Structure to Optoelectronic Device Efficiency. *Chemical Reviews* **2021,** *121* (4), 2230-2291.https://doi.org/10.1021/acs.chemrev.0c01006
49. Mao, L.; Stoumpos, C. C.; Kanatzidis, M. G., Two-Dimensional Hybrid Halide Perovskites: Principles and Promises. *Journal of the American Chemical Society* **2019,** *141* (3), 1171-1190.https://doi.org/10.1021/jacs.8b10851
50. Ksiądzyna, M.; Gągor, A.; Piecha-Bisiorek, A.; Ciżman, A.; Medycki, W.; Jakubas, R., Exploring a Hybrid Ferroelectric with a 1-D Perovskite-Like Structure: Bis(Pyrrolidinium) Pentachloroantimonate(Iii). *Journal of Materials Chemistry C* **2019,** *7* (33), 10360-10370.http://dx.doi.org/10.1039/C9TC02849H
51. Li, Y.; Yang, T.; Liu, X.; Han, S.; Wang, J.; Ma, Y.; Guo, W.; Luo, J.; Sun, Z., A Chiral Lead-Free Photoactive Hybrid Material with a Narrow Bandgap. *Inorganic Chemistry Frontiers* **2020,** *7* (15), 2770-2777.http://dx.doi.org/10.1039/D0QI00546K
52. Ok, K. M.; Min, K. K.; Jo, V.; Kim, S. K.; Shin, I. O., New Organically Templated Noncentrosymmetric Bismuth Chloride: Synthesis, Structure, and Characterization of [N(Ch3)2h2][(Ch3)2nh(Ch2)2nh(Ch3)2][Bicl6]. *Bulletin of the Korean Chemical Society* **2008,** *29* (11), 2273-2376.
53. Elfaleh, N.; Chouaib, H.; Kamoun, S., Bis(3-Azaniumylpropyl)Azanium Hexachloridobismuthate(Iii) Monohydrate. *Acta Crystallographica Section E* **2013,** *69* (12), m666.https://doi.org/10.1107/S1600536813030900
54. Moskwa, M.; Bator, G.; Rok, M.; Medycki, W.; Miniewicz, A.; Jakubas, R., Investigations of Organic–Inorganic Hybrids Based on Homopiperidinium Cation with Haloantimonates(Iii) and Halobismuthates(Iii). Crystal Structures, Reversible Phase Transitions, Semiconducting and Molecular Dynamic Properties. *Dalton Transactions* **2018,** *47* (38), 13507-13522.http://dx.doi.org/10.1039/C8DT03121E
55. Shannon, R., Revised Effective Ionic Radii and Systematic Studies of Interatomic Distances in Halides and Chalcogenides. *Acta Crystallographica Section A* **1976,** *32* (5), 751-767.https://doi.org/10.1107/S0567739476001551
56. Xiao, Z.; Lei, H.; Zhang, X.; Zhou, Y.; Hosono, H.; Kamiya, T., Ligand-Hole in [Sni6] Unit and Origin of Band Gap in Photovoltaic Perovskite Variant Cs2sni6. *Bulletin of the Chemical Society of Japan* **2015,** *88* (9), 1250-1255.https://www.journal.csj.jp/doi/abs/10.1246/bcsj.20150110
57. Kieslich, G.; Sun, S.; Cheetham, A. K., An Extended Tolerance Factor Approach for Organic–Inorganic Perovskites. *Chemical Science* **2015,** *6* (6), 3430-3433.http://dx.doi.org/10.1039/C5SC00961H
58. Fortunato, M.; Bidsorkhi, H. C.; Chandraiahgari, C. R.; Bellis, G. D.; Sarto, F.; Sarto, M. S., Pfm Characterization of Pvdf Nanocomposite Films with Enhanced Piezoelectric Response. *IEEE Transactions on Nanotechnology* **2018,** *17* (5), 955-961.
59. Perdew, J. P.; Burke, K.; Ernzerhof, M., Generalized Gradient Approximation Made Simple. *Phys Rev Lett* **1996,** *77* (18), 3865-3868.
60. Manz, T. A.; Limas, N. G., Introducing Ddec6 Atomic Population Analysis: Part 1. Charge Partitioning Theory and Methodology. *RSC Advances* **2016,** *6* (53), 47771-47801.http://dx.doi.org/10.1039/C6RA04656H
61. Limas, N. G.; Manz, T. A., Introducing Ddec6 Atomic Population Analysis: Part 2. Computed Results for a Wide Range of Periodic and Nonperiodic Materials. *RSC Advances* **2016,** *6* (51), 45727-45747.http://dx.doi.org/10.1039/C6RA05507A
62. Manz, T. A., Introducing Ddec6 Atomic Population Analysis: Part 3. Comprehensive Method to Compute Bond Orders. *RSC Advances* **2017,** *7* (72), 45552-45581.http://dx.doi.org/10.1039/C7RA07400J

63. Perdew, J. P.; Ruzsinszky, A.; Csonka, G. I.; Vydrov, O. A.; Scuseria, G. E.; Constantin, L. A.; Zhou, X.; Burke, K., Restoring the Density-Gradient Expansion for Exchange in Solids and Surfaces. *Physical Review Letters* **2008,** *100* (13), 136406.https://link.aps.org/doi/10.1103/PhysRevLett.100.136406
64. Hush, N. S.; Hobbs, R. J. M., Absorption Spectra of Crystals Containing Transition Metal Ions. In *Progress in Inorganic Chemistry*, 1968; pp 259-486.https://doi.org/10.1002/9780470166116.ch4
65. Li, G.; Camaioni, D. M.; Amonette, J. E.; Zhang, Z. C.; Johnson, T. J.; Fulton, J. L., [Cucln]2−N Ion-Pair Species in 1-Ethyl-3-Methylimidazolium Chloride Ionic Liquid−Water Mixtures: Ultraviolet−Visible, X-Ray Absorption Fine Structure, and Density Functional Theory Characterization. *The Journal of Physical Chemistry B* **2010,** *114* (39), 12614-12622.https://doi.org/10.1021/jp106762b
66. Khan, M. A.; Schwing-Weill, M. J., Stability and Electronic Spectra of the Copper(Ii) Chloro Complexes in Aqueous Solutions. *Inorganic Chemistry* **1976,** *15* (9), 2202-2205.https://doi.org/10.1021/ic50163a041
67. Reinen, D.; Friebel, C., Copper(2+) in 5-Coordination: A Case of a Second-Order Jahn-Teller Effect. 2. Pentachlorocuprate(3-) and Other Cuiil5 Complexes: Trigonal Bipyramid or Square Pyramid? *Inorganic Chemistry* **1984,** *23* (7), 791-798.https://doi.org/10.1021/ic00175a001
68. Wang, Z.-X.; Zhang, H.; Wang, F.; Cheng, H.; He, W.-H.; Liu, Y.-H.; Huang, X.-Q.; Li, P.-F., Superior Transverse Piezoelectricity in a Halide Perovskite Molecular Ferroelectric Thin Film. *Journal of the American Chemical Society* **2020,** *142* (29), 12857-12864.https://doi.org/10.1021/jacs.0c06064
69. Maintz, S.; Deringer, V. L.; Tchougréeff, A. L.; Dronskowski, R., Lobster: A Tool to Extract Chemical Bonding from Plane-Wave Based Dft. *Journal of Computational Chemistry* **2016,** *37* (11), 1030-1035.https://onlinelibrary.wiley.com/doi/abs/10.1002/jcc.24300
70. Zhou, C.; Worku, M.; Neu, J.; Lin, H.; Tian, Y.; Lee, S.; Zhou, Y.; Han, D.; Chen, S.; Hao, A.; Djurovich, P. I.; Siegrist, T.; Du, M.-H.; Ma, B., Facile Preparation of Light Emitting Organic Metal Halide Crystals with near-Unity Quantum Efficiency. *Chemistry of Materials* **2018,** *30* (7), 2374-2378.https://doi.org/10.1021/acs.chemmater.8b00129
71. Aktas, O.; Kangama, M.; Linyu, G.; Catalan, G.; Ding, X.; Zunger, A.; Salje, E. K. H., Piezoelectricity in Nominally Centrosymmetric Phases. *Physical Review Research* **2021,** *3* (4), 043221.https://link.aps.org/doi/10.1103/PhysRevResearch.3.043221
72. Park, H.; Ha, C.; Lee, J.-H., Advances in Piezoelectric Halide Perovskites for Energy Harvesting Applications. *Journal of Materials Chemistry A* **2020,** *8* (46), 24353-24367.http://dx.doi.org/10.1039/D0TA08780G
73. Chen, X.-G.; Song, X.-J.; Zhang, Z.-X.; Li, P.-F.; Ge, J.-Z.; Tang, Y.-Y.; Gao, J.-X.; Zhang, W.-Y.; Fu, D.-W.; You, Y.-M.; Xiong, R.-G., Two-Dimensional Layered Perovskite Ferroelectric with Giant Piezoelectric Voltage Coefficient. *Journal of the American Chemical Society* **2020,** *142* (2), 1077-1082.https://doi.org/10.1021/jacs.9b12368
74. Pandey, R.; Sb, G.; Grover, S.; Singh, S. K.; Kadam, A.; Ogale, S.; Waghmare, U. V.; Rao, V. R.; Kabra, D., Microscopic Origin of Piezoelectricity in Lead-Free Halide Perovskite: Application in Nanogenerator Design. *ACS Energy Letters* **2019,** *4* (5), 1004-1011.
75. Harada, J.; Yoneyama, N.; Yokokura, S.; Takahashi, Y.; Miura, A.; Kitamura, N.; Inabe, T., Ferroelectricity and Piezoelectricity in Free-Standing Polycrystalline Films of Plastic Crystals. *J Am Chem Soc* **2018,** *140* (1), 346-354.https://www.ncbi.nlm.nih.gov/pubmed/29224333
76. Liao, W.-Q.; Zhao, D.; Tang, Y.-Y.; Zhang, Y.; Li, P.-F.; Shi, P.-P.; Chen, X.-G.; You, Y.-M.; Xiong, R.-G., A Molecular Perovskite Solid Solution with Piezoelectricity Stronger Than Lead Zirconate Titanate. *Science* **2019,** *363* (6432), 1206-1210.https://www.science.org/doi/abs/10.1126/science.aav3057
77. Liao, W. Q.; Tang, Y. Y.; Li, P. F.; You, Y. M.; Xiong, R. G., Large Piezoelectric Effect in a Lead-Free Molecular Ferroelectric Thin Film. *J Am Chem Soc* **2017,** *139* (49), 18071-18077.https://www.ncbi.nlm.nih.gov/pubmed/29144132

78. You, Y.-M.; Liao, W.-Q.; Zhao, D.; Ye, H.-Y.; Zhang, Y.; Zhou, Q.; Niu, X.; Wang, J.; Li, P.-F.; Fu, D.-W.; Wang, Z.; Gao, S.; Yang, K.; Liu, J.-M.; Li, J.; Yan, Y.; Xiong, R.-G., An Organic-Inorganic Perovskite Ferroelectric with Large Piezoelectric Response. *Science* **2017,** *357* (6348), 306-309.https://science.sciencemag.org/content/sci/357/6348/306.full.pdf
79. Morrow, D. J.; Hautzinger, M. P.; Lafayette, D. P.; Scheeler, J. M.; Dang, L.; Leng, M.; Kohler, D. D.; Wheaton, A. M.; Fu, Y.; Guzei, I. A.; Tang, J.; Jin, S.; Wright, J. C., Disentangling Second Harmonic Generation from Multiphoton Photoluminescence in Halide Perovskites Using Multidimensional Harmonic Generation. *The Journal of Physical Chemistry Letters* **2020,** *11* (16), 6551-6559.https://doi.org/10.1021/acs.jpclett.0c01720
80. Herman, W. N.; Hayden, L. M., Maker Fringes Revisited: Second-Harmonic Generation from Birefringent or Absorbing Materials. *J. Opt. Soc. Am. B* **1995,** *12* (3), 416-427.http://opg.optica.org/josab/abstract.cfm?URI=josab-12-3-416
81. Sheldrick, G., A Short History of Shelx. *Acta Crystallographica Section A* **2008,** *64* (1), 112-122.https://doi.org/10.1107/S0108767307043930
82. Le Page, Y.; Saxe, P., Symmetry-General Least-Squares Extraction of Elastic Data for Strained Materials from Ab Initio Calculations of Stress. *Physical Review B* **2002,** *65* (10), 104104.https://link.aps.org/doi/10.1103/PhysRevB.65.104104
83. Gajdoš, M.; Hummer, K.; Kresse, G.; Furthmüller, J.; Bechstedt, F., Linear Optical Properties in the Projector-Augmented Wave Methodology. *Physical Review B* **2006,** *73* (4), 045112.https://link.aps.org/doi/10.1103/PhysRevB.73.045112
84. Baroni, S.; Resta, R., Ab Initio Calculation of the Macroscopic Dielectric Constant in Silicon. *Physical Review B* **1986,** *33* (10), 7017-7021.https://link.aps.org/doi/10.1103/PhysRevB.33.7017

TOC graphic

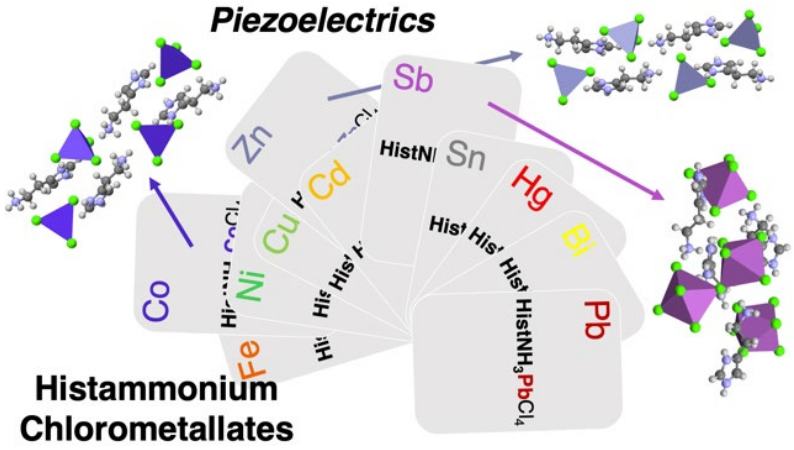

TOC SYNOPSIS

To provide new insights in understanding the influence of B site cation on structure in chlorometallate materials of the form $AB^{n+}Cl_{n+2}$, incorporating histammonium ($HistNH_3$) dications and various transition metal and main group B site cations. $HistNH_3CoCl_4$, $HistNH_3ZnCl_4$ had no inversion symmetry and were isostructural, however, the Zn-based material had a much higher piezoelectric response. Computational studies indicated material response differences were due to differences in dipole magnitude and M-Cl contribution to the valence band maximum.